

Ab initio free energies of liquid metal alloys: Application to the phase diagrams of Li-Na and K-NaYang Huang and Michael Widom *Department of Physics, Carnegie Mellon University, Pittsburgh, Pennsylvania 15213, USA*Michael C. Gao *National Energy Technology Laboratory, Albany, Oregon 97321, USA*

(Received 12 May 2021; revised 15 September 2021; accepted 1 December 2021; published 11 January 2022)

Comparison of free energies between different phases and different compositions underlies the prediction of alloy phase diagrams. To allow direct comparison, consistent reference points for the energies or enthalpies are required, and the entropy must be placed on an absolute scale, yielding *absolute* free energies. Here we derive absolute free energies of liquids from *ab initio* molecular dynamics by combining the directly simulated enthalpies with an entropy derived from simulated densities and pair correlation functions. As an example of the power of this method we calculate the phase diagrams of two binary alkali metal alloys, Li-Na and K-Na, revealing a critical point and liquid-liquid phase separation in the former case, and a deep eutectic in the latter. Good agreement with experimental data demonstrates the power of this simple method.

DOI: [10.1103/PhysRevMaterials.6.013802](https://doi.org/10.1103/PhysRevMaterials.6.013802)**I. INTRODUCTION**

The free energy of a compound, $G = H - TS$, depends on both the enthalpy H and the entropy S . Shifting H by a constant value has no consequence because only free energy *differences* enter into thermodynamics. Although the values are arbitrary, comparing the free energies of competing phases is facilitated if consistently chosen reference values are applied to the enthalpies. By thermodynamic convention, the reference point for enthalpy of a compound is chosen as the sum of the enthalpies of all constituent elements in their stable state at standard temperature and pressure. However, other choices can be equally valid, in principle. For example, one could choose the enthalpy as calculated within density functional theory (DFT) at temperature $T = 0$ K as the reference point, placing high-temperature enthalpies as calculated from *ab initio* molecular dynamics (AIMD) on a well-defined absolute scale. In contrast, since the entropy enters the free energy multiplied by T , its actual value cannot be chosen arbitrarily. Indeed, a unique reference point for the entropy is provided by the third law; namely, S must vanish at $T = 0$ K. The combination of enthalpy on a well-defined relative scale and entropy on an absolute scale yields absolute free energy.

Knowledge of absolute entropy $S(E)$ is equivalent to knowledge of the configurational density of states $\Omega(E)$. Histogram [1] and entropic sampling methods [2] such as Wang-Landau [3] calculate $\Omega(E)$ up to an unknown constant factor, yielding relative but not absolute entropies. In some special discrete cases, such as lattice models where the total number of states is known, $\Omega(E)$ can be normalized yielding absolute entropy.

Most methods to compute absolute free energy rely on connecting the free energy of interest to some reference state of known free energy. Thermodynamic integration [4] calculates $\partial G/\partial\lambda$ through simulation (λ is some parameter in

the Hamiltonian) then numerically integrates this derivative. Thermodynamic perturbation theory [5,6] expresses $G(\lambda)$ as a low-order Taylor series expansion. Umbrella sampling [7] and the Bennett acceptance ratio method [8] provide increased computational efficiency to these basic approaches, as do other schemes [9]. In practice, the thermodynamic integration requires reversible paths so that the free energy and its derivatives are well defined. This is sometimes referred to as the slow-growth approach [10–12]. Jarzynski's identity $\exp(-\beta\Delta F) = \langle \exp(-\beta W_\lambda) \rangle$ holds even for nonequilibrium transitions and allows for evolution over short time durations, which is known as the “fast-growth” method [13].

Other methods build the free energy through sequential addition of particles. The exact scanning approach [14–16] computes the partial density of states $\rho(\alpha_k|\alpha_{k-1}\cdots\alpha_1)$ where the set $\{\alpha_j\}$ is an ordered sequence of states containing successively more particles. Similarly, the particle insertion method [17] calculates the free energy difference of a k -atom system and a $(k-1)$ -atom system (i.e., the chemical potential), although without explicitly calculating the density of states.

The empirical CALPHAD approach [18,19], proposes analytical free energy models for the Gibbs free energy $G(x, T)$ of a compound with composition x . Starting from the ideal free energy $G_{\text{ideal}} = H_{\text{ideal}} - TS_{\text{ideal}}$, CALPHAD models the excess free energy in a series of Redlich-Kister polynomials [20] with coefficients obtained from experimental information such as heat capacity and phase diagrams. The result is a set of free energy functions in analytic form that can be used to interpolate the free energy into compositions for which no data are available.

We recently developed an approximate method to calculate absolute entropy of liquid metals from AIMD simulations of their densities and pair correlation functions [21,22]. Since entropies cannot otherwise be derived directly from simulations, our method provides a feasible approach to

calculate the absolute entropy, and hence the absolute free energy, with high accuracy and reduced computational effort. As a demonstration of the utility of absolute free energy and the power of our calculational approach, we apply the method to calculate the free energies of two binary alkali metal alloy systems, Li-Na and K-Na. These examples are chosen because, despite the seeming chemical similarity, the two systems exhibit very different phase behaviors. Li and Na are nearly immiscible, both in the solid state and in the liquid below a critical point at $T = 578$ K. In contrast, K-Na compounds remain liquid below the melting points of elemental Na and K, forming a deep eutectic at 33% Na and $T = 260$ K (-13°C). The low melting point of K_2Na (often abbreviated as “NaK”) makes the liquid alloy useful as a coolant for nuclear reactors [23] and other applications. The immiscibility of Na in Li makes it potentially useful for suppression of dendrites in Li-ion batteries [24].

In the following we first describe our simulation methods, including the manner in which we obtain absolute enthalpies and entropies. Then we validate the methods by comparing our calculated densities for pure elemental liquids with experimental values, and our absolute entropies with values tabulated in the NIST-JANAF tables [25]. Finally, we present our predicted phase diagrams of Li-Na and K-Na and compare with published experimental results, finding that they show good agreement. We find a high positive energy of mixing between Li and Na atoms which leads to phase separation at moderately high temperatures, with a critical point for phase mixing at higher temperatures. For the K-Na system, the energy of mixing is still positive, but it is relatively weak. In consequence the entropy dominates the free energy. After incorporating the Gibbs free energies of competing solid phases, we observe a deep eutectic transition at temperatures below 0°C .

II. METHODS

We simulate liquid K-Na and Li-Na using *ab initio* energies and forces to accurately reproduce their configurational ensembles. Different strategies are used for elemental and binary metallic systems. For pure elements standard *ab initio* molecular dynamics (AIMD) simulations are performed. For binary alloys, we supplement AIMD with additional Monte Carlo chemical species swapping steps [26] in order to accelerate the sampling of diverse configurations. Enthalpies are taken directly from the *ab initio* total energies, while entropies are obtained from integrals of correlation functions [21,22]. We carry out our simulations in canonical ensembles although our entropy model is expressed in the grand canonical ensemble, relying on locality of the correlations to achieve ensemble independence [27].

Specific simulated temperatures and compositions are chosen to cover the relevant soluble regions of the Li-Na and K-Na phase diagrams. Only soluble phases are chosen to avoid contaminating our data with multiple phases and interfacial free energies. We then fit the Gibbs free energy to an analytical model from which we derive the phase diagrams by computing the convex hull of $G(x, T)$. Individual data points are given in the Supplemental Material [28].

A. *Ab initio* molecular dynamics and Monte Carlo

Our AIMD simulations apply electronic density functional theory as implemented in the Vienna *Ab initio* Simulation Package (VASP [29,30]). First-principles energies and forces are calculated using the PBE generalized gradient approximation [31,32]. MD time steps are set at 1 fs with the temperature controlled in the *NVT* ensemble using a Nosé thermostat. We take a plane-wave basis set with a cutoff energy of $E = 300$ eV. Semicore electrons are included in the pseudopotentials for potassium atoms and sodium atoms while only valence electrons are considered for lithium atoms. We employ simulation cells of 300 atoms for K-Na and 500 atoms for Li-Na. Justification for these decisions is presented in Appendix A.

Simulations at a given temperature and composition are pre-annealed for a minimum of 1 ps, until the onset of equilibrium energy fluctuations, followed by data acquisition for a minimum of 2 ps. We take equilibrated configurations from high-temperature runs as initial conditions for lower temperature runs. To predict the density at a given temperature and composition, we monitor the total pressure at five different volumes, and then find the volume at which the pressure vanishes by fitting to a quadratic polynomial.

In binary systems, we additionally perform Metropolis Monte Carlo by testing a randomly chosen interchange of two atoms’ chemical species and accepting the change with probability $\exp(-\Delta E/k_B T)$. We attempt one species swap every 10 MD steps. On average, a total number of 300 atomic swap attempts are made with a acceptance rates around 15%. Supplementing AIMD with Monte Carlo (MCMD [26]) accelerates the approach to equilibrium and enhances the configurational diversity of the simulated ensemble, as discussed in Appendix B.

B. Entropy

We calculate absolute entropies directly from MCMD simulations performed at the temperatures, densities, and compositions of interest by evaluating the leading terms in an expansion of the entropy in a series of progressively higher-order correlation functions [27,33–35]. This method has been previously validated for elemental liquid Al and Cu, and applied to the AlCu binary liquid alloy [21,22].

The quantum mechanically derived absolute entropy of the ideal gas is

$$S_{\text{ideal}}/k_B = \frac{5}{2} - \sum_{\alpha} x_{\alpha} \ln(\rho x_{\alpha} \lambda_{\alpha}^3), \quad (1)$$

where α denotes atomic species, $\lambda_{\alpha} = \sqrt{h^2/2\pi m_{\alpha} k_B T}$ is the thermal de Broglie wavelength of species α , x_{α} is its fraction, and ρ is total atomic number density. Note that S_{ideal} contains the entropy of mixing

$$S_{\text{mix}}/k_B = - \sum_{\alpha} x_{\alpha} \ln(x_{\alpha}). \quad (2)$$

The leading term in the correlation function expansion is the single-body entropy $S_1 = S_{\text{ideal}} - k_B$, with the difference arising from interchange of multiple atoms [22,27]. The two-body

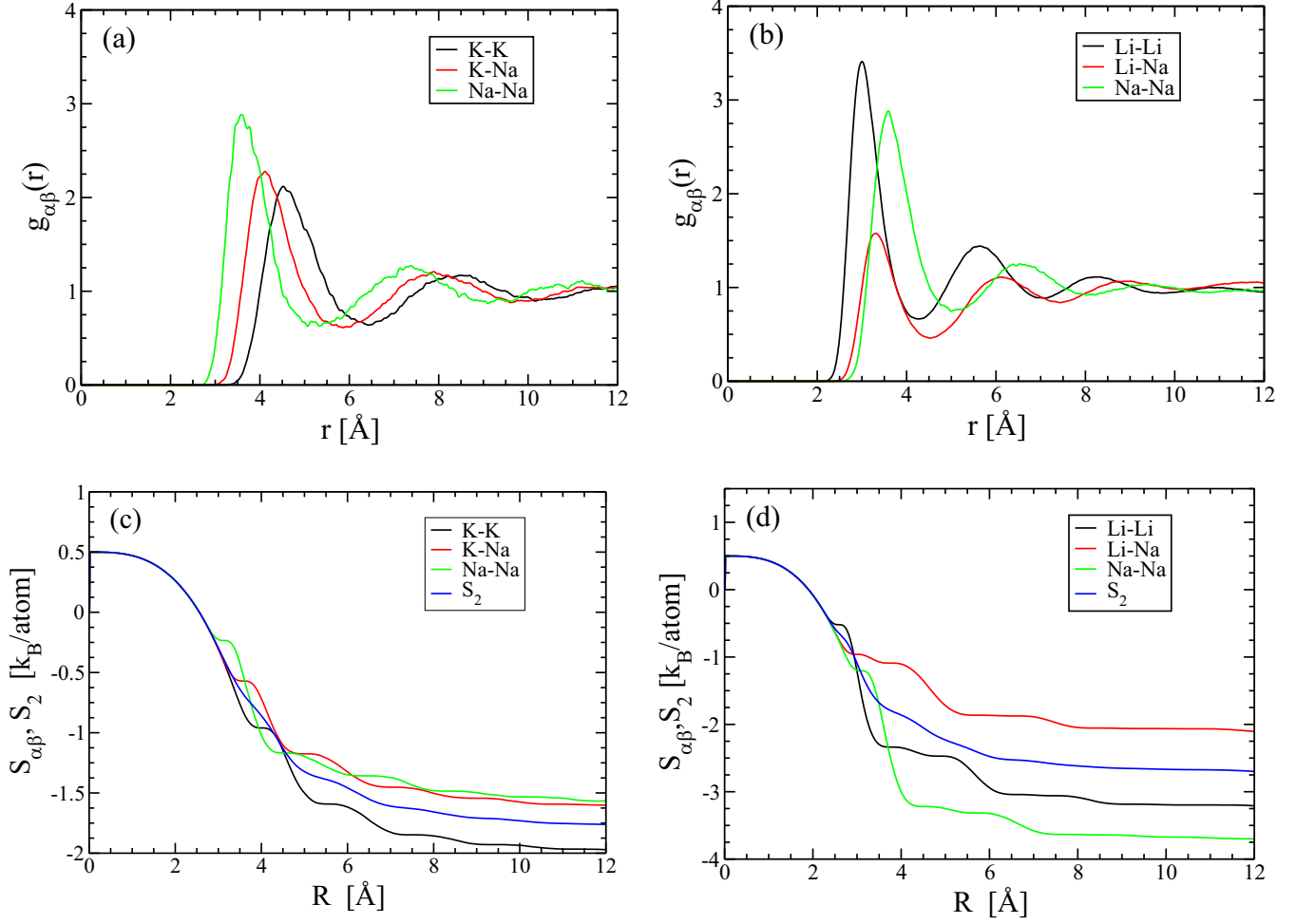


FIG. 1. Radial distribution functions $g_{\alpha\beta}(r)$ of (a) K_2Na and (b) Li_2Na calculated by MCMD for for $N = 300$ atoms at $T = 473$ K. (c) and (d) Two-body entropies $S_{\alpha\beta}$ and S_2 [see Eq. (5)] integrated up to distance R .

corrections to S_1 include a fluctuation term

$$S_{\text{fluct}} = \frac{1}{2} \sum_{\alpha,\beta} x_{\alpha}x_{\beta} \left(1 + \rho \int_0^R dr 4\pi r^2 [g_{\alpha\beta}(r) - 1] \right) \quad (3)$$

that is positive but very small (it is proportional to the isothermal compressibility) and an information term

$$S_{\text{info}} = -\frac{1}{2} \rho \sum_{\alpha,\beta} x_{\alpha}x_{\beta} \int_0^R dr 4\pi r^2 g_{\alpha\beta}(r) \ln g_{\alpha\beta}(r) \quad (4)$$

that is negative-definite and reflects the entropy reduction due to the information content of the pair correlation functions. We approximate the total entropy as $S \approx S_1 + S_2$ with $S_2 = S_{\text{fluct}} + S_{\text{info}}$. Note that S_2 can be decomposed into partial contributions for each species pair,

$$S_2 = \sum_{\alpha\beta} x_{\alpha}x_{\beta} S_{\alpha\beta},$$

$$S_{\alpha\beta} = \frac{1}{2} \left(1 + \rho \int_0^R dr 4\pi r^2 [g_{\alpha\beta}(r) \ln g_{\alpha\beta}(r) + g_{\alpha\beta}(r) - 1] \right). \quad (5)$$

Figures 1(a) and 1(b) show correlation functions of K_2Na and Li_2Na , respectively. Each correlation function vanishes

within its atomic core, and thereafter exhibits decaying oscillations. Positions of the first peaks vary in accordance with relative atomic diameters. The oscillation frequencies are similar for each combination of species, suggesting a universal origin of oscillation. Indeed it is known that alkali metals possess long-range oscillatory potentials [36] with a frequency of twice the Fermi wave number [37]. For valence-1 elements with atomic volume $v = 1/\rho$, the Fermi wave numbers $k_F = (3\pi^2/v)^{1/3}$ evaluate to $k_F = 0.75$ and 1.01 \AA^{-1} for K_2Na and Li_2Na , respectively. These values roughly match the k_F values 0.84 and 1.04 \AA^{-1} inferred from observed oscillation frequencies of the correlations. A hard-sphere distribution function with hard-sphere radius $R = (3v/4\pi)^{1/3}$ also matches the frequencies but does not reproduce the detailed shapes of the correlation functions.

Because the oscillations decay, the integrals in Eq. (5) converge as the upper limit of integration R increases, as shown in Figs. 1(c) and 1(d). We take the values at $R = 12 \text{ \AA}$ for our values of S_2 . $S_{\alpha\beta}$ and S_2 are negative-definite (in the large- R limit) reflecting the loss of entropy due to the correlations. The entropy loss is larger for Li_2Na than for K_2Na because of the strong chemical order that prefers like neighbors (Li-Li and Na-Na), while this effect is nearly absent in the case of K_2Na .

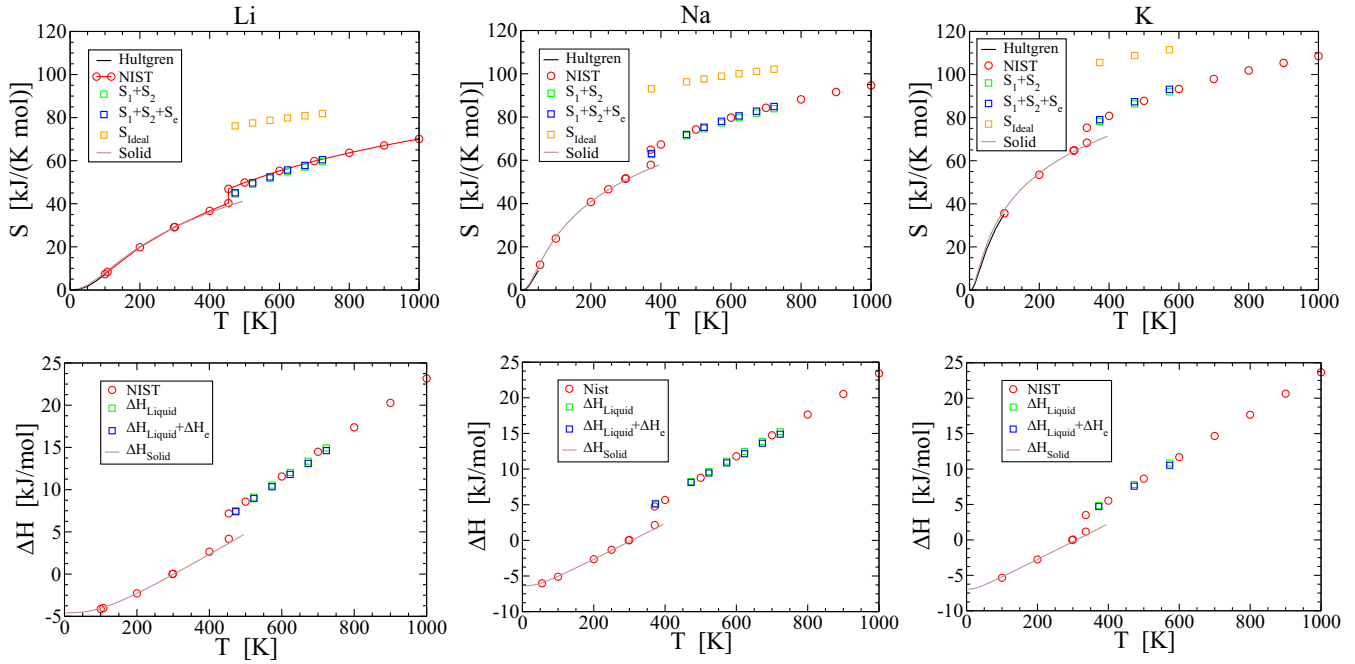


FIG. 2. Comparison between calculated and experimental entropies (top row) and enthalpies (bottom row) for Li, Na, and K (from left to the right). Experimental values labeled NIST come from the NIST-JANAF standard reference database [25], while experimental entropies at low temperatures are integrated from the heat capacities C_p tabulated by Hultgren [41]. Three liquid state entropy approximations are represented: the ideal gas entropy S_{ideal} , and the sum of the one-body and two-body entropies $S_1 + S_2$ with and without electronic entropy S_e . Solid state entropies S_{solid} are derived from PHONOPY.

C. Electronic free energy

Electronic free energies are included in every case to supplement our systematic calculations of thermodynamic quantities of alkali metals. Electronic free energies at finite temperature are obtained from the DFT-predicted electronic density of state $D(\epsilon)$ as discussed in [38]. Electronic contributions to the relative free energies ΔG are relatively small compared with ΔG itself.

D. Interpolation

Because we carry out simulations at discrete temperatures and compositions, but we wish to determine phase boundaries as continuously varying functions of temperature, we require a method to interpolate the enthalpy and entropy. To compute the phase diagrams it suffices to model $\Delta H(x, T)$ and $\Delta S(x, T)$ relative to their values at the concentration end points $x = 0$ and $x = 1$. Then the compositions x where $\Delta G(x, T) = \Delta H(x, T) - T\Delta S(x, T)$ lies above its own convex hull determine the phase coexistence regions.

We fit the excess enthalpy $\Delta H(x, T)$ and two-body term $S_2(x, T)$ to a quartic polynomial

$$f(x, T) = x(1-x)[a(T)x + b(T)x + C(T)x^2], \quad (6)$$

where $a(T)$, $b(T)$, and $c(T)$ are linear functions of T , resulting in 6 fitting parameters for each thermodynamic function f . The enthalpy and entropy satisfy the constraints $f(0) = 0$ and $f(1) = 0$, while the quadratic function of composition in the brackets captures asymmetry. The simple linear temperature

dependence approximation is designed for accuracy over a narrow temperature range. This approximation works well for single-species liquid enthalpies as shown in Fig. 2. The S_1 term is calculated from Eq. (1) using a quartic function to fit the composition-dependent density. By this approach, we capture the logarithmic singularities of the entropy near $x = 0$ and $x = 1$.

E. Solid phases

The Gibbs free energies of competing phases must be included to determine the global phase diagrams. These phases are body-centered-cubic solid phases of pure elements, and a Laves phase (Pearson hP12, Strukturbericht C14) KNa_2 binary phase. The Gibbs free energy for a solid phase includes the vibrational free energy G^v , the electronic free energy G^e , and a configurational free energy G^c . In principle the configurational term includes contributions due to chemical and vacancy disorder [38]; however, experimental evidence suggests that the K-Li-Na solid phases are nearly stoichiometric, so we simply approximate G^c with the enthalpy of the fully relaxed (i.e., $T = 0$ K) structure. First-principles vibrational free energy calculations use the same pseudopotentials and exchange-correlation function as for the liquid simulations, but with an increased plane-wave cutoff energy of 500 eV and an increased electronic k -mesh density so that we may obtain accurate interatomic force constants. The Gibbs free energies at finite temperatures are calculated within the quasiharmonic approximation using PHONOPY [39,40]. The differing cutoff energies and k meshes result in an offset between solid

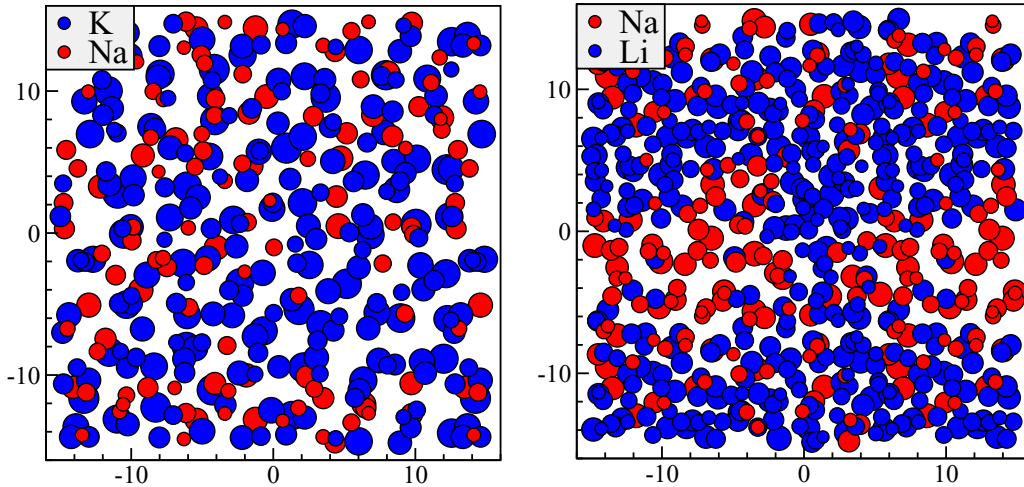


FIG. 3. Snapshots of typical MCMD simulated configurations for (left) K_2Na and (right) Li_2Na at $T = 473$ K. Positions are plotted from back to front, with diameters indicating depth (large at the back and small in front, to enhance visibility). Spatial units are Å.

and liquid enthalpies, which we correct by matching our calculated enthalpy differences between 200 K and 500 K to experiment.

III. RESULTS

A. Pure elemental Li, Na, and K

The calculated entropies and enthalpies of pure elemental Li, Na, and K in their solid and liquid states are plotted in Fig. 2 and compared to experimental values from the NIST-JANAF tables [25]. After shifting our reference point for enthalpy to set $\Delta H = 0$ at $T = 293.15$ K, the calculated enthalpies are in excellent agreement with experiment across both solid and liquid states, with deviations of 1 kJ/mol or less. Solid state entropies are also in excellent agreement with experiment at low temperatures but show a slight deficit of less than 1 J/(K mol) just below the melting temperatures. We compare three different models for the liquid state entropy. The ideal gas model S_{ideal} substantially overestimates the entropy, while the single-body entropy S_1 yields an improvement, and the two-body correction S_2 brings the value close to experiment, but slightly below. Finally, a small contribution from the electronic entropy provides an excellent match to experiment at temperatures above melting. A small deficit remains in the liquid entropy close to the melting point that is presumably due to three- and four-body correlations [22].

B. Binary K-Na

As shown in our simulation snapshot of K_2Na at $T = 473$ K in Fig. 3 (left), K and Na atoms are uniformly distributed, indicating a homogeneous liquid state. We confirm a stable mixture of liquid K-Na alloy at $T = 473$ K and $x = 33\%$. The stability of the liquid alloy is confirmed by our calculated enthalpies, entropies, and Gibbs free energies as plotted in Fig. 4. The internal energy of the compound is positive, which could indicate phase separation, but the amplitude of its peak is substantially below the amplitude of the peak in the Li-Na system, and far below the magnitude of

TS . Values of S_1 contain the density ρ , which varies monotonically and smoothly with composition, and also contains the entropy of mixing S_{mix} . Hence $-T\Delta S_1$ is negative and strongly convex. Note that although S_2 is negative-definite, we find that $-T\Delta S_2$, defined relative to the pure elements, is negative and seemingly is also convex. As a result, the total Gibbs free energy is dominated by entropy and is convex over all compositions, resulting in continuous miscibility of K and Na at 473 K. We would expect phase separation below $T = 189$ K based on extrapolation of ΔG to low temperatures, but this is preempted by the eutectic transition to the solid phases, as we now discuss.

We compare the free energy of the liquid phase with its competing solid phases in order to predict the composition- and temperature-dependent $K_{1-x}Na_x$ phase diagram as shown in Fig. 4(c). K-Na has three known low-temperature phases: elemental K ($x = 0$), elemental Na ($x = 1$), and the KNa_2 Laves phase ($x = 2/3$). In the experimental phase diagram, a deep eutectic transition occurs at $x_E \approx 33\%$ and $T_E \approx 260$ K, where the K-Na alloy exists in the liquid state at temperatures below the melting points of elemental K and Na. In our predicted phase diagram, a eutectic transition is found near $T = 268$ K and $x = 40.3\%$, not very far from the experimental position.

The deviation of these values from the experimental transition might be an effect of the systematic error in prediction via DFT or it might be due to our approximations for the entropy. To understand which is most responsible, we compare the predicted melting points (i.e., the temperatures at which solid and liquid free energies cross) with experiment as seen at $x = 0$ and 1 in Fig. 4(c). Our calculated melting temperatures of elemental K and Na are approximately 359 K and 355 K, respectively, which differ somewhat from the experimental values of 336 K and 370 K. An alternative approach to calculating melting temperatures via DFT using interface pinning predicts the melting point of elemental Na to be $T_m \approx 354$ K [45] which is very close to our predicted 355 K. This agreement between our approach and interface pinning suggests the discrepancy of both predictions compared with experiment may lie primarily within DFT.

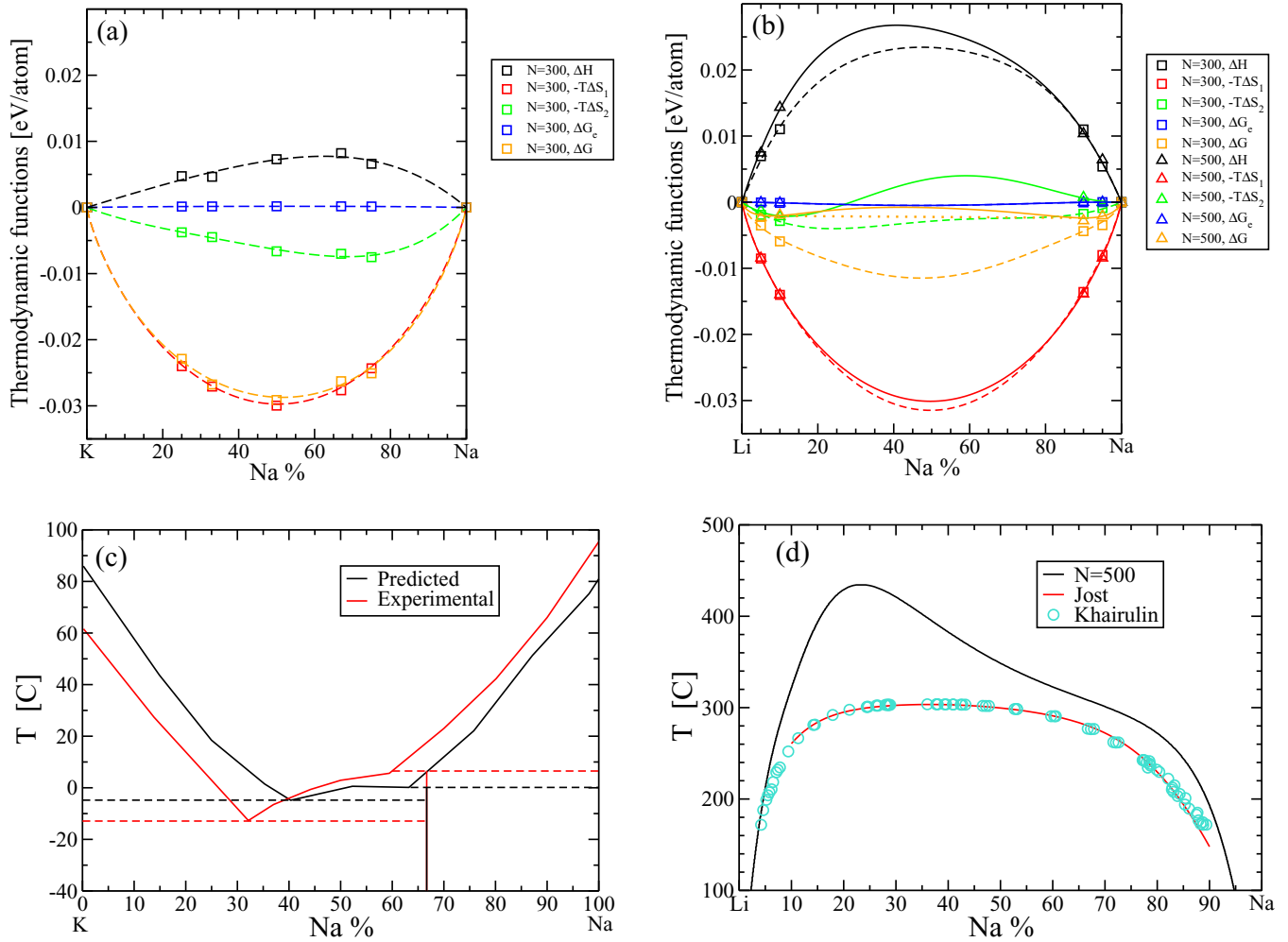


FIG. 4. Top row: Thermodynamic functions of (a) K-Na and (b) Li-Na at $T = 473$ K, relative to values for pure elements. S_1 and S_2 are the one- and two-body contributions to the entropy. Data points are individual simulations, while curves are fits to Eq. (6) (dashed are from $N = 300$ atoms, solid from $N = 500$). The orange dotted line in (b) shows the convex hull of $G(x)$. Bottom row: Predicted and experimental phase diagrams [42–44] of (c) K-Na and (d) Li-Na.

C. Li-Na

We present a snapshot of a 300-atom Li_2Na system at $T = 473$ K in Fig. 3 (right). The snapshot shows clear phase separation into an Na-rich region and an Li-rich region that mutually coexist in equilibrium. The separation is also evident in the correlation functions in Fig. 1(b), where the amplitudes of the first two peaks of the Li-Na pair correlation function are substantially smaller than those of Li-Li and Na-Na, indicating effective Li-Na repulsion.

In order to understand how internal energies and entropies contribute to the total free energies and drive the system toward phase separation, we plot our calculated enthalpy, entropy, and Gibbs free energy for $\text{Li}_{1-x}\text{Na}_x$ in Fig. 4(b). The energy cost of mixing Li and Na is large compared to that of mixing K and Na [Fig. 4(a)], and similar in magnitude but opposite in sign to $-TS$. The resulting free energy lacks convexity and hence explains the separation of liquid Li and Na at low and moderately high temperatures. Specifically, $G(x)$ lies above its own convex hull over the interval from $x = 0.07$ to $x = 0.90$ [see dotted orange line in Fig. 4(b)].

A liquid alloy in this composition range will phase separate into a mixture of those two end point compositions. Note that we only use data at compositions that lie within our predicted single-phase regions.

Collecting data similar to those of Fig. 4(b) at higher temperatures (see Fig. 8 in Appendix C), we then fit the temperature evolution of the phase boundaries. Figure 4(d) compares our predicted phase coexistence region with the experimental results labeled Jost [43] and Khairulin [44]. This figure is based on simulated data from $T = 523$ K and 573 K. Note that we reproduce the boundary qualitatively, including the asymmetry showing greater solubility at the Na-rich end, with the notable exception of the vicinity of the critical point. The difficulty in the vicinity of the critical point is not a surprise because the expected singularities in the thermodynamic functions cannot be represented within our polynomial form [Eq. (6)]. Similarly, the diverging correlation lengths near the critical point cannot be accommodated in our finite-size simulation cells. Critical exponents of Li-Na have recently been measured experimentally and match

expectations for the three-dimensional Ising universality class [44].

In addition to the Li-Na phase separation, a eutectic transition (not shown) occurs at $x_{\text{Na}} \approx 97\%$ and $T \approx 290$ K and a monotectic transition near the melting point of Li. Both features are also reported in the experimental phase diagram [46].

IV. CONCLUSIONS

In summary, we systematically studied thermodynamic properties of solid and liquid K-Na and Li-Na metallic alloys at finite temperature and zero pressure. The Gibbs free energies of bcc K, Li, and Na, and Laves phase KNa_2 , were calculated in the quasiharmonic approximation as implemented in PHONOPY [39,40]. Standard *ab initio* molecular dynamics and Monte Carlo/molecular dynamics simulations modeled the liquid alloys. Absolute entropies in the liquid state were obtained as functionals of simulated densities and pair correlation functions. We note that a similar approach is possible in the solid state also [21,47]. At $T = 473$ K we observed phase separation in Li_2Na in contrast to phase mixing in K_2Na , and these observations were justified by explicit calculation of the composition-dependent absolute Gibbs free energy $G(x)$ that revealed nonconvexity in the case of Li-Na.

Extending our calculations to other temperatures, we predicted composition-temperature phase diagrams that agreed well with experiment in most respects. Specifically, we obtained a deep eutectic transition in K-Na and liquid-liquid phase separation in Li-Na. Our principal shortcoming was our inability to accurately model the critical point for Li-Na phase separation. We attribute this difficulty to the thermodynamic singularities and diverging correlation length that characterize the critical point [44].

Although the present study exclusively addresses the special case of liquid Li-Na and K-Na alloys, our methods generalize to more complex liquid metals. This could prove useful in conjunction with design of multicomponent high-entropy alloys [48] where knowledge of the liquidus and

solidus temperatures would be helpful. If we have C chemical species, in a simulation cell of N atoms, then at fixed N the available data $D_{\alpha\beta}$ relevant to a given correlation function $g_{\alpha\beta}(r)$ falls off as $1/C$. To maintain accuracy as C grows, in the face of diminishing data, would require run times to grow as C^2 . Further, correct prediction of liquid-solid phase equilibria depends on prior knowledge of the coexisting solid phases.

The principal limiting factor in the present approach is our truncation of the entropy expansion at the level of pair correlations. This is likely not sufficient for molecular liquids, and liquids with strong covalent bonding. Additionally, in order to converge the integrals in Eqs. (3)–(5) the simulation cell size must exceed the range of the correlation functions. We already saw in Fig. 4 that the diverging correlation length limited our accuracy close to the critical point of Li-Na. Similar difficulties would occur due to long-range Coulomb interactions in ionic liquids.

ACKNOWLEDGMENTS

Y.H. and M.W. acknowledge support from U.S. Department of Energy Grant No. DE-SC0014506. M.C.G. acknowledges support from the U.S. Department of Energy’s Fossil Energy Crosscutting Technology Research Program through the NETL Research and Innovation Center’s Advanced Alloy Development Field Work Proposal. We benefited from computer time at the Pittsburgh Supercomputer Center under XSEDE Grant No. DMR160149 and at the National Energy Research Scientific Computing Center (NERSC) using Award No. ERCAP0015745.

APPENDIX A: OPTIMIZATION OF CALCULATION PARAMETERS

Density functional theory calculations make numerous approximations that affect the accuracy of its predictions. Here we test choices of numerous calculational details that affect our results, seeking to achieve a balance between accuracy and computational efficiency. Because the enthalpy and entropy both depend sensitively on the density of the liquid, and experimental data on density are readily available and presumably

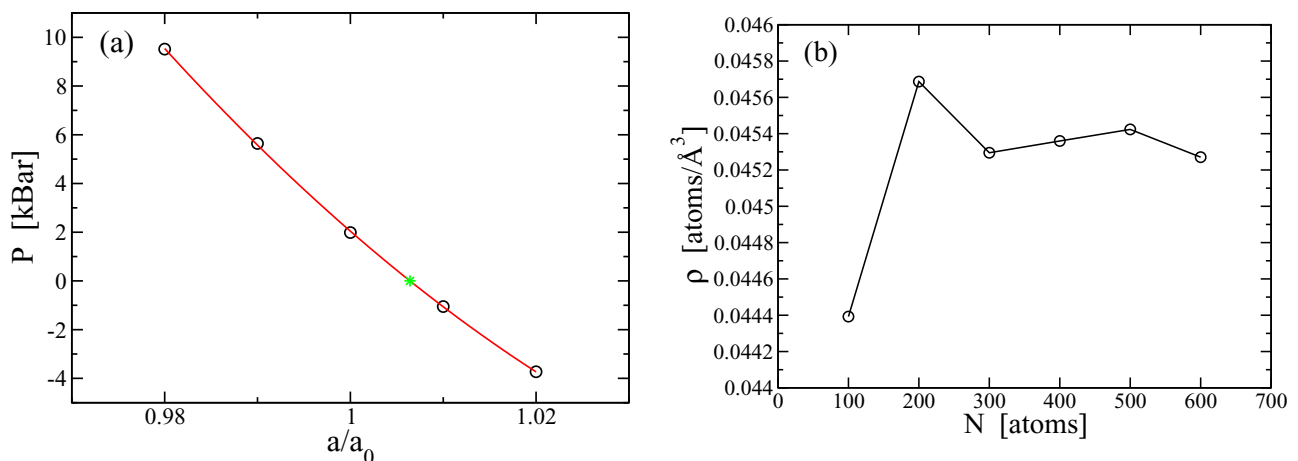


FIG. 5. (a) AIMD-calculated pressure vs cell size a for $N = 300$ Li atoms at $T = 473$ K. Circles are individual runs, curve is a quadratic fit, and the star marks our fitted $P = 0$. (b) Variation of predicted density $\rho = 300/a^3$ with respect to number of atoms N .

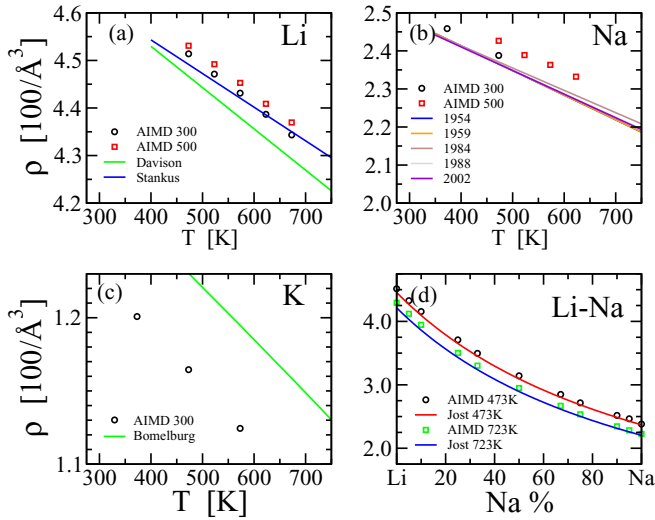
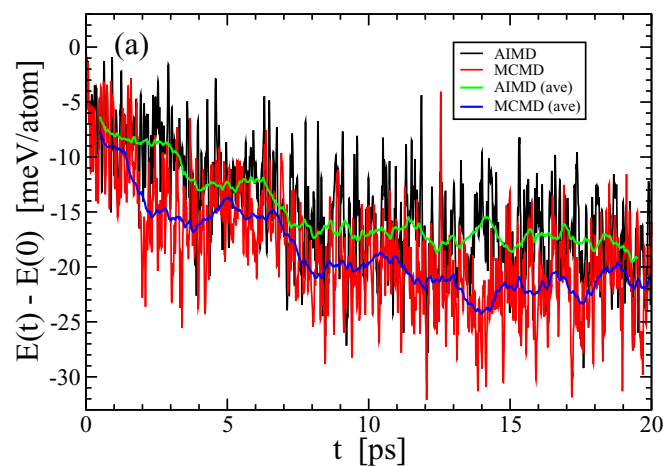


FIG. 6. Comparison of AIMD and MCMD predicted densities with experimental data. All runs use a single k point, energy cutoff of 300 eV, and PAW potentials in the PBE gradient approximation. (a) Li with $N = 300$ and 500 atoms. References are Davison [51], Stankus [52]. (b) Na with $N = 300$ and 500 atoms. References 1954–2002 come from [53]. (c) K with $N = 300$ atoms. (d) Li-Na at 473 K and 723 K comparing AIMD and experiment [43].

reliable, we take the accuracy of our predicted density as a measure of accuracy overall.

1. Size of simulation cell

Previously, in our study of liquid Al [22], we observed oscillations in the predicted density as a function of the size of the simulation cell. This effect was related to the commensurability of cell lattice constant a_0 with the oscillation frequency of the spatial correlation functions. To assess this behavior for alkali metals we simulated elemental liquid Li using $N = 100$ –400 atom cells. The runs were performed using the valence-1 PAW_PBE-type pseudopotential



“Li 17Jan2003” and we employed a plane-wave energy cutoff of 180 eV that exceeds the default by the recommended 30%, and a single k point. For each number of atoms we performed runs at $T = 473$ K taking several cell sizes a in the vicinity of the expected optimum a_0 . We fit the average pressure (including the kinetic component [49]) at each size to a quadratic and solved for the equilibrium volume at $P = 0$ as illustrated in Fig. 5(a). Oscillations die off with increasing size, and on the basis of Fig. 5(b) we judge that we obtain accuracy of around 0.2% when $N = 300$. Since the ideal gas entropy varies logarithmically with respect to density, this translates into an uncertainty of around $0.002k_B$ in the ideal gas component of the entropy, and will be a relatively small component of our overall uncertainty.

When we simulated the Li-Na and K-Na binaries, we found that the $N = 300$ atom cells exhibited spontaneous phase separation (see, e.g., main text Fig. 3) over wide ranges of composition, even at temperatures far above the expected critical temperature. In contrast, cells with $N = 500$ did not show this behavior, and in fact revealed only localized indications of separation below the critical temperature. Thus we adopt $N = 300$ -atom cells for K-Na and $N = 500$ -atom cells for Li-Na. Further, our thermodynamic modeling is restricted to data obtained from temperature-composition combinations at which phase separation is not predicted.

2. Cutoff energy

The incompleteness of the plane-wave basis set creates systematic errors in the calculated pressure (the Pulay stress [50]) that diminish as the plane-wave energy cutoff increases. Different elements, and even different pseudopotentials for the same element, have very different default energy cutoffs. The defaults are 140.000 eV for “Li 17Jan2003,” 116.731 eV for “K_pv 17Jan2003,” and 259.561 eV for “Na_pv 19Sep2006.” The “_pv” subscripts indicate that p semicore electrons are treated as valence. Computational cost grows as the cube of the number of plane waves, which itself grows as the 3/2 power of the energy cutoff, leading to rapid growth of cost versus

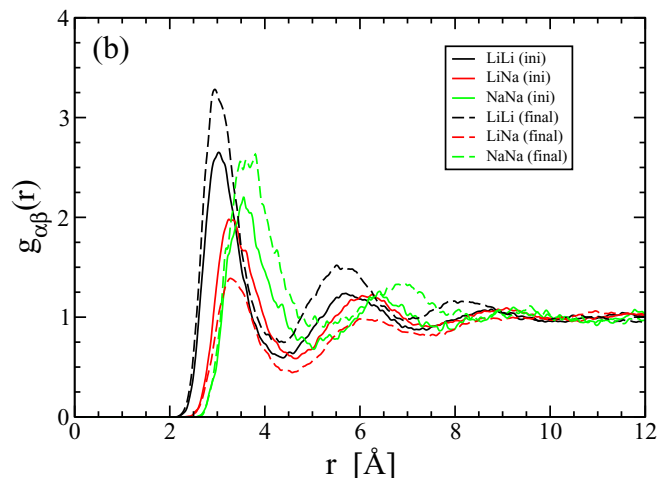


FIG. 7. (a) Equilibration of total energy for AIMD compared with MCMD showing instantaneous values and running averages over intervals of 1 ps. The Li_2Na liquid has $N = 300$ atoms at $T = 573$ K. Monte Carlo swaps are attempted every 10 fs. (b) Pair distribution functions $g_{\alpha\beta}(r)$ averaged over initial and final 1 ps of MCMD simulation.

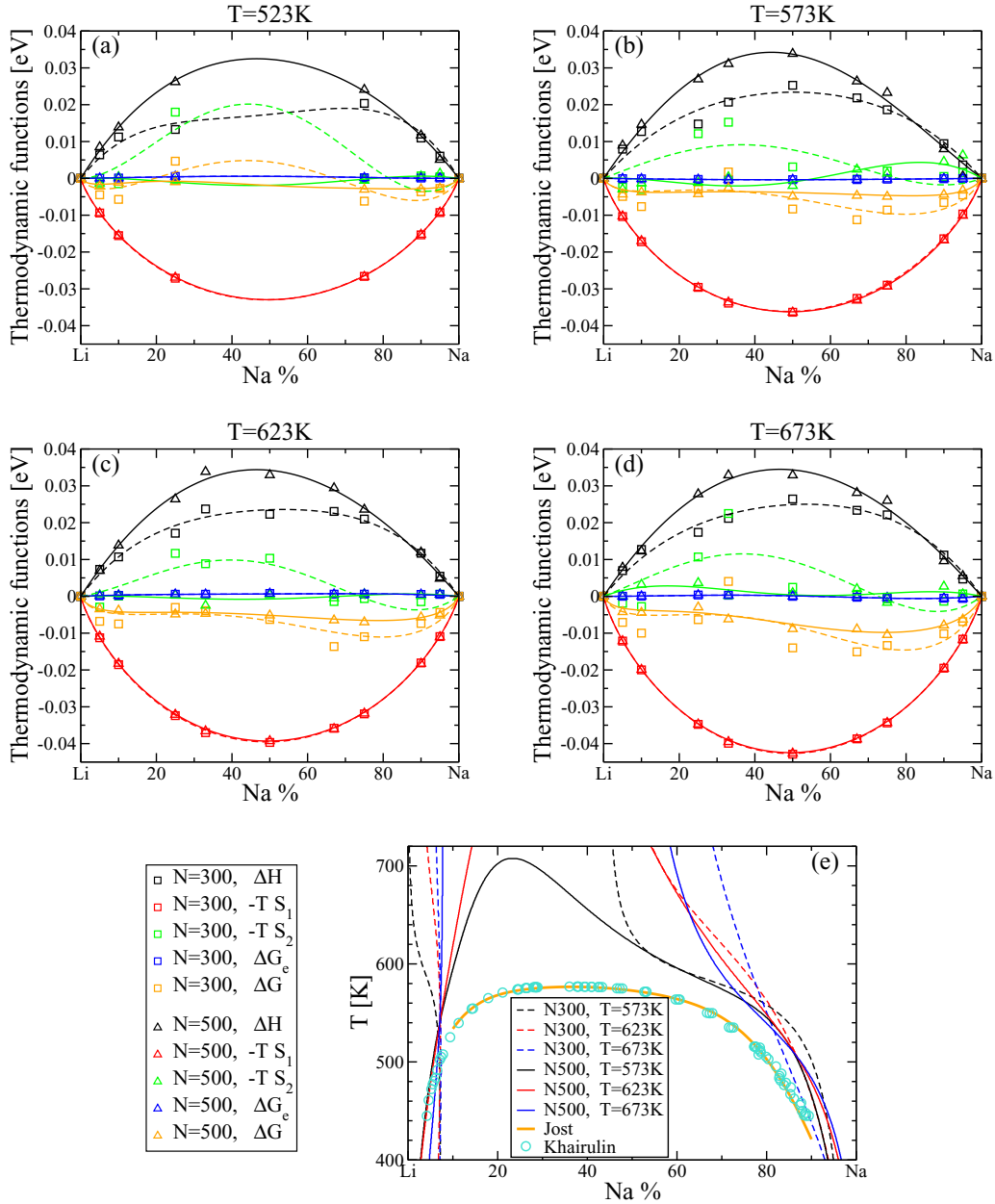


FIG. 8. (a)–(d) Thermodynamic functions of Li-Na at temperatures 523–673 K, and (e) predicted phase boundaries. Thermodynamic functions are enthalpy H (black), one-body entropy $-TS_1$ (red), two-body entropy $-TS_2$ (green), electronic free energy G_e (blue), and total free energy G (orange). Data points are AIMD simulation (squares for $N = 300$ atoms, triangles for $N = 500$). Curves (dashed for $N = 300$ atoms and solid for $N = 500$) are fits to Eq. (6). (e) Predicted phase boundaries for Li-Na including all data up to and including temperatures 573–673 K from simulation sizes $N = 300$ and 500 atoms. Curve labeled Jost is a model fit to experiment [43], while explicit data points are taken from Khairulin [44].

cutoff, yet consistency of calculated energies requires that the applied energy cutoff be uniform across different compositions. Since the Na potential requires the highest energy cutoff for both the Li-Na and K-Na alloy systems, we explore the sensitivity of the density of Na to the energy cutoff. Testing values 260, 300, and 340 eV, with systems of $N = 300$ atoms at $T = 473$ K, we obtained densities of 0.02948, 0.02378, and 0.02381 atoms/Å³. Thus we settle on a cutoff of 300 eV. Note the experimental value is around 0.0237 [see Fig. 6(b)].

Figure 6(d) illustrates the composition-dependent densities for Li-Na at two temperatures and compare with experiment

[43]. Our predictions follow the experimental trends, while remaining slightly high.

Note that the predicted density of K drops with increasing energy cutoff, and converges to nearly 5% below the experimental value at this cutoff. The situation is marginally improved if we switch to the “K_{sv}” potential, but not sufficiently to compensate for the increased electron count.

3. XC functional

The choice of exchange correlation functional can lead to systematic errors in the density. We compared the local

density approximation (LDA) with the PBE generalized gradient approximation and with PBEsol for a system of $N = 300$ Li atoms at $T = 473$ K using an energy cutoff of 300 eV and a single k point. These yielded densities of 0.04535, 0.04516, and 0.04511 atoms/Å³, for LDA, PBE, and PBEsol, respectively, compared with experimental values that range from 0.0444 to 0.0448. All three overestimate the density. PBEsol proves only marginally better than PBE, and we prefer PBE because it is more widely used. To test whether this is caused by neglect of the Li core electrons, we tested the valence-3 “Li_sv 10Sep2004” potential at energy cutoff 650 eV (30% above its default of 499.034 eV) and found density 0.0462, which is far above the experimental value. Thus we settle on the PBE functional and stick with our decision to use the valence-1 Li potential.

4. Uncertainties in thermodynamic quantities

Our calculations are subject to both systematic and statistical errors. Density functional theory itself relies on the approximate exchange-correlation functional, leading to systematic errors that we do not attempt to quantify, beyond noting that differing choices of functional had modest influence on the density as discussed in Sec. A 3, while DFT may lead to errors in the vicinity of 15 K for the melting point of Na as discussed in Sec. III B. We truncate our expansion of the entropy at the pair level, systematically omitting three- and higher-body correlations. This may be the reason that our entropy falls below experiment close to the melting point [22,47], as seen in Fig. 2. We restrict our simulations to certain finite sizes, leading to errors on the density as shown in Fig. 5, but also leading to premature phase separation in Li-Na even at high temperatures above the critical point, when the correlation length grows beyond our simulated cell size (see Fig. 8).

To estimate our statistical errors, we break our runs into three segments and evaluate the standard error on the assumption of uncorrelated errors. For K₂Na at $T = 473$ K we find statistical errors of order 1 meV/atom in both the enthalpy H and the entropy $-TS_2$. However, these are anticorrelated so that the statistical error on G is of order 0.4 meV/atom. These statistical errors are in general agreement with the scatter of

data points around our smoothed fitting curves as seen in Figs. 4 and 8.

APPENDIX B: ACCELERATED SAMPLING

Hybrid Monte Carlo/molecular dynamics (MCMD [26]) is applied in order to accelerate the sampling of the configurational ensemble. This method supplements conventional molecular dynamics, in which the structure evolves continuously through diffusion of atoms, with discrete interchanges of pairs of atoms of differing chemical species. Although the Monte Carlo steps are less important in the liquid state than in the solid state, where diffusion is nearly unachievable, we still see an improvement in equilibration time. Figure 7(a) graphs the evolution in total energy for a 300-atom Li₂Na liquid at $T = 573$ K in which atomic species have initially been randomly interchanged then briefly annealed under conventional AIMD. The energy drops more rapidly under MCMD as species swaps allow more rapid growth of clusters of like-species atoms. Once equilibrium is achieved, around 10 ps, MCMD continues to enhance the diversity of the sampled ensemble, while AIMD has not yet reached equilibrium. Figure 7(b) illustrates the evolution of pair correlations during the MCMD simulation, showing a drop in mixed Li-Na species pairs and corresponding growth in like-species pairs.

APPENDIX C: DETAILED RESULTS FOR Li-Na

This section presents detailed results for the simulated thermodynamic functions of Li-Na at various temperatures and numbers of atoms, as illustrated in Figs. 8(a)–8(d). Non-convexity of the total Gibbs free energy $G(x)$ predicts phase separation at each temperature, though the uncertainties on our fits to Eq. (6) are sufficient to render those predictions doubtful especially at the higher temperatures. Consequently, our predicted phase boundaries place the critical points for phase mixing far above the experimental value [see Fig. 8(e)], especially for $N = 300$ atoms, where visible phase separation (see Fig. 3) persists to the highest temperatures. The experimentally observed asymmetry in the coexistence curve is respected in every predicted phase boundary.

-
- [1] A. M. Ferrenberg and R. H. Swendsen, *Phys. Rev. Lett.* **63**, 1195 (1989).
- [2] J. Lee, *Phys. Rev. Lett.* **71**, 211 (1993).
- [3] F. Wang and D. P. Landau, *Phys. Rev. Lett.* **86**, 2050 (2001).
- [4] J. G. Kirkwood, *J. Chem. Phys.* **3**, 300 (1935).
- [5] R. W. Zwanzig, *J. Chem. Phys.* **22**, 1420 (1954).
- [6] C. Peter, C. Oostenbrink, A. van Dorp, and W. F. van Gunsteren, *J. Chem. Phys.* **120**, 2652 (2004).
- [7] G. Torrie and J. Valleau, *J. Comput. Phys.* **23**, 187 (1977).
- [8] C. H. Bennett, *J. Comput. Phys.* **22**, 245 (1976).
- [9] L.-F. Zhu, B. Grabowski, and J. Neugebauer, *Phys. Rev. B* **96**, 224202 (2017).
- [10] T. K. Woo, P. M. Margl, J. C. W. Lohrenz, P. E. Blöchl, and T. Ziegler, *J. Am. Chem. Soc.* **118**, 13021 (1996).
- [11] T. K. Woo, P. M. Margl, P. E. Blöchl, and T. Ziegler, *J. Phys. Chem. B* **101**, 7877 (1997).
- [12] H. Hu, R. H. Yun, and J. Hermans, *Mol. Simul.* **28**, 67 (2002).
- [13] D. A. Hendrix and C. Jarzynski, *J. Chem. Phys.* **114**, 5974 (2001).
- [14] H. Meirovitch, *J. Phys. A* **15**, L735 (1982).
- [15] H. Meirovitch, *J. Chem. Phys.* **89**, 2514 (1988).
- [16] H. Meirovitch, S. Chelvaraja, and R. P. White, *Curr. Protein Pept. Sci.* **10**, 229 (2009).
- [17] B. Widom, *J. Chem. Phys.* **39**, 2808 (1963).
- [18] L. Kaufman and H. Bernstein, *Computer Calculation of Phase Diagrams* (Academic Press, 1970).
- [19] H. Lukas, S. G. Fries, and B. Sundman, *Computational Thermodynamics: The Calphad Method* (Cambridge University Press, Cambridge, 2007).

- [20] O. Redlich and A. T. Kister, *Ind. Eng. Chem.* **40**, 345 (1948).
- [21] M. C. Gao and M. Widom, *J. Phys. Chem. B* **122**, 3550 (2018).
- [22] M. Widom and M. Gao, *Entropy* **21**, 131 (2019).
- [23] S. Chetal, in *Encyclopedia of Materials: Science and Technology*, edited by K. J. Buschow, R. W. Cahn, M. C. Flemings, B. Ilschner, E. J. Kramer, S. Mahajan, and P. Veysiere (Elsevier, Oxford, 2001), pp. 6361–6364.
- [24] J. K. Stark, Y. Ding, and P. A. Kohl, *J. Electrochem. Soc.* **158**, A1100 (2011).
- [25] T. Allison, JANAF Thermochemical Tables, NIST Standard Reference Database 13, <http://janaf.nist.gov>.
- [26] M. Widom, W. P. Huhn, S. Maiti, and W. Steurer, *Metall. Mater. Trans. A* **45**, 196 (2014).
- [27] A. Baranyai and D. J. Evans, *Phys. Rev. A* **40**, 3817 (1989).
- [28] See Supplemental Material at <http://link.aps.org/supplemental/10.1103/PhysRevMaterials.6.013802> for individual data points of the Gibbs free energies, enthalpies, one-body entropies and two-body entropies of Li-Na at $T = 473$ K, 523 K, 573 K, and 623 K, and K-Na at $T = 273$ K, 373 K, and 473 K.
- [29] G. Kresse and J. Furthmüller, *Phys. Rev. B* **54**, 11169 (1996).
- [30] G. Kresse and D. Joubert, *Phys. Rev. B* **59**, 1758 (1999).
- [31] J. P. Perdew, K. Burke, and M. Ernzerhof, *Phys. Rev. Lett.* **77**, 3865 (1996).
- [32] P. E. Blöchl, *Phys. Rev. B* **50**, 17953 (1994).
- [33] H. S. Green, *The Molecular Theory of Fluids* (North-Holland, Amsterdam, 1952).
- [34] H. J. Raveché, *J. Chem. Phys.* **55**, 2242 (1971).
- [35] D. C. Wallace, *J. Chem. Phys.* **87**, 2282 (1987).
- [36] A. Paskin and A. Rahman, *Phys. Rev. Lett.* **16**, 300 (1966).
- [37] J. Hafner, *From Hamiltonians to Phase Diagrams: The Electronic and Statistical-Mechanical Theory of sp-Bonded Metals and Alloys* (Springer, Berlin, 1986).
- [38] M. Widom, *J. Mater. Res.* **33**, 2881 (2018).
- [39] A. Togo and I. Tanaka, *Scr. Mater.* **108**, 1 (2015).
- [40] A. Togo, L. Chaput, I. Tanaka, and G. Hug, *Phys. Rev. B* **81**, 174301 (2010).
- [41] T. Massalski, H. Okamoto, P. Subramanian, and L. Kacprzak, editors, *Binary Alloy Phase Diagrams*, 2nd ed. (ASM International, Materials Park, OH, 1990).
- [42] C. W. Bale, in T. Massalski, H. Okamoto, P. Subramanian, and L. Kacprzak, editors, *Binary Alloy Phase Diagrams*, 2nd ed. (ASM International, Materials Park, OH, 1990), Vol. 3, p. 2376.
- [43] J. Jost, D. Heydt, J. Spehr, and H. Ruppertsberg, *J. Phys.: Condens. Matter* **6**, 321 (1994).
- [44] R. A. Khairulin, R. N. Abdullaev, and S. V. Stankus, *J. Eng. Thermophys.* **28**, 472 (2019).
- [45] U. R. Pedersen, F. Hummel, G. Kresse, G. Kahl, and C. Dellago, *Phys. Rev. B* **88**, 094101 (2013).
- [46] C. W. Bale, in T. Massalski, H. Okamoto, P. Subramanian, and L. Kacprzak, editors, *Binary Alloy Phase Diagrams*, 2nd ed. (ASM International, Materials Park, OH, 1990), Vol. 3, p. 2448.
- [47] D. M. Nicholson, C. Y. Gao, M. T. McDonnell, C. C. Sluss, and D. J. Keffer, *Entropy* **23**, 234 (2021).
- [48] R. Feng, C. Zhang, M. C. Gao, Z. Pei, F. Zhang, Y. Chen, D. Ma, K. An, J. D. Poplawsky, L. Ouyang, Y. Ren, J. A. Hawk, M. Widom, and P. K. Liaw, *Nat. Commun.* **12**, 4329 (2021).
- [49] P. Ganesh and M. Widom, *Phys. Rev. Lett.* **102**, 075701 (2009).
- [50] P. Pulay, *Mol. Phys.* **17**, 197 (1969).
- [51] H. W. Davison, *Compilation of Thermophysical Properties of Liquid Lithium*, Tech. Rep. (NASA Lewis Research Center, 1968), NASA TN D-4650.
- [52] S. V. Stankus, R. A. Khairulin, and A. G. Mozgovoï, *High Temp.* **49**, 187 (2011).
- [53] V. Sobolev, *Database of Thermophysical Properties of Liquid Metal Coolants for GEN-IV*, Tech. Rep. (Belgian Nuclear Research Center SCK-CEN, 2011).